

The Synchrosqueezing algorithm: a robust analysis tool for signals with time-varying spectrum

Eugene Brevdo, Neven S. Fućkar, Gaurav Thakur, and Hau-Tieng Wu

Abstract

We analyze the Synchrosqueezing transform, a consistent and invertible time-frequency analysis tool that can identify and extract oscillating components (of time-varying frequency and amplitude) from regularly sampled time series. We first describe a fast algorithm implementing the transform. Second, we show Synchrosqueezing is robust to bounded perturbations of the signal. This stability property extends the applicability of Synchrosqueezing to the analysis of nonuniformly sampled and noisy time series, which are ubiquitous in engineering and the natural sciences. Numerical simulations and examples in paleoclimatology show that Synchrosqueezing provides a natural way to analyze and filter a variety of signals.

I. INTRODUCTION

Synchrosqueezing is a tool designed to extract and compare oscillatory components of signals that arise in complex systems. It provides a powerful method for analyzing signals with time-varying behavior and can give insight into the structure of their constituent components. Such signals $f(t)$ have the general form

$$f(t) = \sum_{k=1}^K f_k(t) + e(t), \quad (1)$$

E. Brevdo is with the Department of Electrical Engineering, Princeton University e-mail: ebrevdo@math.princeton.edu.

N.S. Fućkar is with the International Pacific Research Center, University of Hawaii, Honolulu, Hawaii.

H.-T. Wu is with the Department of Mathematics, Princeton University.

G. Thakur is with the Program in Applied and Computational Mathematics, Princeton University.

where each component $f_k(t) = A_k(t) \cos(\phi_k(t))$ is an oscillating function, possibly with smoothly time-varying amplitude and frequency, and $e(t)$ represents noise or observation error. The goal is to extract the amplitude factor $A_k(t)$ and the Instantaneous Frequency (IF) $\phi'_k(t)$ for each k .

Signals of the form (1) arise naturally in engineering and scientific applications, where it is often important to understand their spectral properties. Many time-frequency (TF) transforms exist for analyzing such signals, such as the Short Time Fourier Transform (STFT), Wavelet Transform, and Wigner-Ville distribution [1], but these methods can fail to capture key short-range characteristics of the signals. As we will see, Synchrosqueezing deals well with such complex data.

Synchrosqueezing is a TF transform that is ostensibly similar to the family of time-frequency reassignment (TFR) algorithms, methods used in the estimation of IFs in signals of the form given in (1). TFR analysis originates from a study of the STFT, which smears the energy of the superimposed IFs around their center frequencies in the spectrogram. TFR analysis “reassigns” these energies to sharpen the spectrogram [2], [3]. However, there are some significant differences between Synchrosqueezing and most standard TFR techniques.

Synchrosqueezing was originally introduced in the context of audio signal analysis [4]. In [5], it was further analyzed theoretically as an alternative way to understand the *Empirical Mode Decomposition* (EMD) algorithm [6]. EMD has proved to be a useful tool for analyzing and decomposing natural signals. Like EMD, Synchrosqueezing can extract and clearly delineate components with time varying spectrum. Furthermore, like EMD, and unlike most TFR techniques, it allows individual reconstruction of these components.

The purpose of this paper is threefold. We first describe the Synchrosqueezing transform in detail and highlight the subtleties of a new fast numerical implementation. Second, we show both numerically and theoretically that Synchrosqueezing is stable under bounded signal perturbations. It is therefore robust to noise and to errors incurred by preprocessing using approximations, such as interpolation. Finally, we combine these ideas and visit open problems in the paleoclimate of the last 2.5 Myr, where Synchrosqueezing provides improved insights. We compare a calculated solar flux index with a deposited $\delta^{18}O$ paleoclimate proxy over this period. Synchrosqueezing cleanly delineates the orbital cycles of the solar radiation, provides an interpretable representation of the orbital signals of $\delta^{18}O$, and improves our understanding of the effect that the solar flux distribution has had on the global climate. Compared to previous analyses of these data, the Synchrosqueezing representation provides more robust and precise estimates in the time-frequency plane.

The paper is organized as follows. We first describing Synchrosqueezing, and in §III we provide a fast

new implementation¹. In §IV we prove that Synchrosqueezing analysis and reconstruction are stable to bounded perturbations. In §V, we numerically compare Synchrosqueezing to other common transforms, and provide examples of its stability properties. Finally, in §VI we focus on the paleoclimate example.

II. SYNCHROSQUEEZING: ANALYSIS

Synchrosqueezing is performed in three steps. First, the Continuous Wavelet Transform (CWT) $W_f(a, b)$ of $f(t)$ is calculated [7]. Second, an initial estimate of the FM-demodulated frequency, $\omega_f(a, b)$, is calculated on the support of W_f . Finally, this estimate is used to squeeze W_f via reassignment; we thus get the Synchrosqueezing representation $T_f(\omega, b)$. Synchrosqueezing is invertible: we can calculate f from T_f . Our ability to extract individual components stems from filtering f by keeping energies from specific regions of the support of T_f during reconstruction.

Note that Synchrosqueezing, as originally proposed [4], estimates the FM-demodulated frequency from the wavelet representation $W_f(a, b)$ before performing reassignment. However, it can be adapted to work on “on top of” many invertible transforms (e.g. the STFT [8]). We focus on the original wavelet version as described in [5].

We now detail each step of Synchrosqueezing, using the harmonic signal $h(t) = A \cos(\Omega t)$ for motivation. As a visual aid, Fig. 1 shows each step on the signal $h(t)$ with $A = 1$ and $\Omega = 4\pi$. Note that Figs. 1(b,d) show that Synchrosqueezing is more “precise” than the CWT.

A. CWT of $f(t)$

For a given mother wavelet ψ , the CWT of f is given by $W_f(a, b) = \int_{-\infty}^{\infty} f(t) a^{-1/2} \overline{\psi\left(\frac{t-b}{a}\right)} dt$, where a is the scale and b is the time offset. We assume that ψ has fast decay, and that its Fourier transform $\widehat{\psi}(\xi) = (2\pi)^{-1/2} \int_{-\infty}^{\infty} \psi(t) e^{-i\xi t} dt$ is approximately zero in the negative frequencies: $\widehat{\psi}(\xi) \approx 0$ for $\xi < 0$, and is concentrated around some positive frequency $\xi = \omega_0$ [5]. Many wavelets have these properties (several examples and compared in §A). For $h(t)$, the harmonic signal above, upon applying our assumptions we get $W_h(a, b) = \frac{1}{2\sqrt{2\pi}} A a^{1/2} \overline{\widehat{\psi}(a\Omega)} e^{ib\Omega}$.

B. Calculate the FM-demodulated frequency $\omega(a, b)$

The wavelet representation of the harmonic signal $h(t)$ (with frequency Ω) will have its energy spread out in the time-scale plane around the line $a = \omega_0/\Omega$, and this frequency will be encoded in the phase

¹The Synchrosqueezing Toolbox for MATLAB, and the codes used to generate all of the figures in this paper, are available at <http://math.princeton.edu/~ebrevdo/synsq/>.

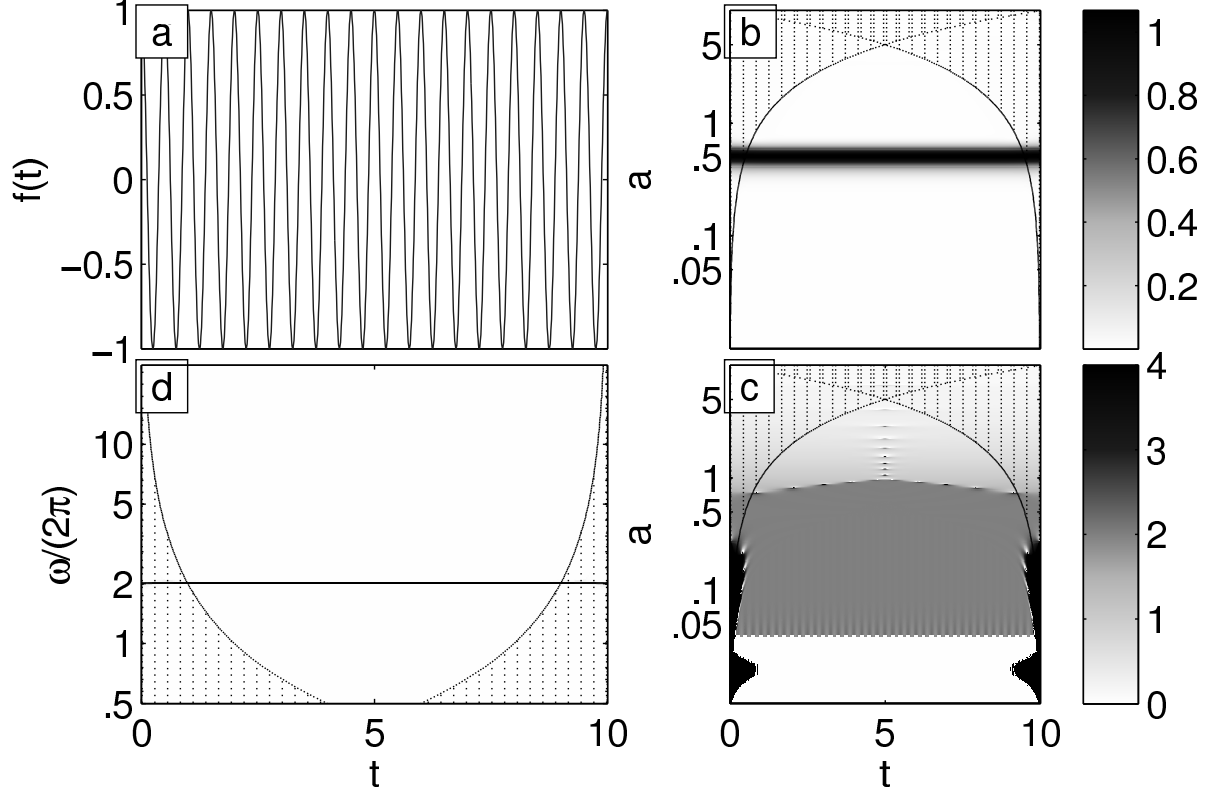


Fig. 1. Synchronsqueezing example for $h(t) = \cos(4\pi t)$. Clockwise: a) $h(t)$, sampled, $n = 1024$ points. b) CWT of h , $|W_h|$. c) FM-demodulated frequency from W_h , ω_h . d) Synchronsqueezing of h : $|T_h|$; line at $w_i \approx 2$.

[4], [5]. In those regions where $|W_h| > 0$ we would like to remove the effect of the Wavelet on this frequency. We perform a type of FM demodulation by taking derivatives: $(W_h(a, b))^{-1} \partial_b W_h(a, b) = i\Omega$. This simple model leads to an estimate of the frequency in the time-scale plane:

$$\omega_f(a, b) = \begin{cases} \frac{-i\partial_b W_f(a, b)}{W_f(a, b)} & |W_f(a, b)| > 0 \\ \infty & |W_f(a, b)| = 0 \end{cases}. \quad (2)$$

C. Squeezing in the time-frequency plane: $T_f(\omega, b)$

The final step of Synchronsqueezing is reassigning energy in the time-scale plane to the TF plane according to the frequency map $(a, b) \rightarrow (\omega(a, b), b)$. Reassignment follows from the inversion property of the CWT: when $f(t)$ is real,

$$f(b) = 2\mathcal{R}_\psi^{-1} \Re \left(\int_0^\infty W_f(a, b) a^{-3/2} da \right), \quad (3)$$

where $\mathcal{R}_\psi = \sqrt{2\pi} \int_0^\infty \xi^{-1} \widehat{\psi}(\xi) d\xi$ is a normalizing constant.

We first break up the integrand in (3) according to the FM-demodulated frequency estimate ω_f . Define frequency divisions $\{w_l\}_{l=0}^{\infty}$ s.t. $w_0 > 0$ and $w_{l+1} > w_l$ for all l . Further, let the frequency bin \mathcal{W}_l be the set of points $w' \in \mathbb{C}$ closer to w_l than to any other w'_l . We define the Discrete-Frequency Wavelet Synchrosqueezing transform of f as:

$$T_f(w_l, b) = \int_{\{a: \omega_f(a, b) \in \mathcal{W}_l\}} W_f(a, b) a^{-3/2} da. \quad (4)$$

In other words, $T_f(w_l, b)$ is the “volume” of the frequency preimage set $\mathcal{W}_l^{-1}(b) = \{a : \omega_f(a, b) \in \mathcal{W}_l\}$ under the signed measure $\mu_{f,b}(a) = W_f(a, b) a^{-3/2} da$.

This definition has several favorable properties. First, it allows us to reconstruct f from T_f :

$$f(b) = 2\mathcal{R}_\psi^{-1} \Re \left(\sum_l T_f(w_l, b) \right). \quad (5)$$

Second, for the harmonic signal $h(t)$, with $\omega_h(a, b) = \Omega$, there will be a single \hat{l} such that $w_{\hat{l}}$ is closest to $\omega_h(a, b)$. From (3), we have $h(b) = 2 \Re \left(\mathcal{R}_\psi^{-1} T_h(w_{\hat{l}}, b) \right)$. Further, the magnitude of T_h is proportional to that of $h(t)$: $|T_h(w_{\hat{l}}, b)| = \frac{|A|}{2\pi} |\mathcal{R}_\psi|$.

More generally, for a wide class of signals with slowly varying $A_k(t)$ and well separated $\phi'_k(t)$, given a sufficiently fine division of the frequency bins $\{w_l\}$, each of the K components can be well concentrated into its own “curve” in the TF plane (see Thm. IV.1 below). This allows us to analyze such signals: by looking at $|T_f(w, b)|$ to identify and extract the curves, and to reconstruct their associated components.

III. A FAST IMPLEMENTATION

In practice, we observe the vector $\tilde{f} \in \mathbb{R}^n$, $n = 2^{L+1}$, where L is a nonnegative integer. Its elements, $\tilde{f}_m, m = 0, \dots, n-1$, correspond to a uniform discretization of $f(t)$ taken at the time points $t_m = t_0 + m\Delta t$. To prevent boundary effects, we pad \tilde{f} on both sides (using, e.g., reflecting boundary conditions).

We now describe a fast numerical implementation of Synchrosqueezing. The speed of our algorithm lies in two key steps. First, we calculate the Discrete Wavelet Transform (DWT) of the vector \tilde{f} using the Fast Fourier Transform (FFT). Second, we discretize the squeezing operator T in a way that lends itself to a fast numerical implementation.

A. DWT of sampled signal \tilde{f}

The DWT samples the CWT W_f at the locations (a_j, t_m) , where $a_j = 2^{j/n_v} \Delta t$, $j = 1, \dots, Ln_v$, and the number of voices n_v is a user-defined “voice number” parameter [9] (we have found that $n_v = 32$

works well). The DWT of \tilde{f} can be calculated in $O(n_v n \log_2^2 n)$ operations using the FFT. We outline the steps below.

First note that $W_f(a, b) = \left[a^{-1/2} \overline{\psi(-t/a)} * f(t) \right] (b)$, where $*$ denotes convolution over t . In the frequency domain, this relationship becomes: $\widehat{W}_f(a, \xi) = a^{1/2} \widehat{f}(\xi) \widehat{\psi}(a\xi)$. We use this to calculate the DWT, $\widetilde{W}_{\tilde{f}}(a_j, t_m)$. Let \mathcal{F}_n (\mathcal{F}_n^{-1}) be the standard (inverse) circular Discrete Fourier Transform. Then

$$\widetilde{W}_{\tilde{f}}(a_j, \cdot) = \mathcal{F}_n^{-1} \left((\mathcal{F}_n \tilde{f}) \odot \widehat{\psi}_j \right). \quad (6)$$

Here \odot denotes elementwise multiplication and $\widehat{\psi}_j$ is an n -length vector with $(\widehat{\psi}_j)_m = a_j^{1/2} \widehat{\psi}(a_j \xi_m)$; ξ_m are samples in the unit frequency interval: $\xi_m = 2\pi m/n$, $m = 0, \dots, n-1$.

B. A Stable Estimate of ω_f : $\widetilde{\omega}_{\tilde{f}}$

We first require a slight modification of the FM-demodulated frequency estimate (2),

$$\omega_f(a, b) = \Im \left((W_f(a, b))^{-1} \partial_b W_f(a, b) \right). \quad (7)$$

This definition is equivalent to (2) when Synchronsqueezing is performed via (4), and simplifies the algorithm.

In practice, signals have noise and other artifacts due to, e.g., sampling errors, and the phase of W_f is unstable when $|W_f| \approx 0$. As such the user should choose some $\gamma > 0$ (we often use $\gamma \approx 10^{-8}$) as a hard threshold on $|W_f|$. We define the numerical support of $\widetilde{W}_{\tilde{f}}$, on which ω_f can be estimated:

$$\widetilde{\mathcal{S}}_{\tilde{f}}^\gamma(m) = \left\{ j : \left| \widetilde{W}_{\tilde{f}}(a_j, t_m) \right| > \gamma \right\}, \text{ for } m = 0, \dots, n-1.$$

The estimate of ω_f , $\widetilde{\omega}_{\tilde{f}}$, can be calculated by taking differences of $\widetilde{W}_{\tilde{f}}$ with respect to m before applying (7), but we provide a more direct way. Let Using the property $\widehat{\partial_b W_f}(a, \xi) = i\xi \widehat{W_f}(a, \xi)$, we estimate the FM-demodulated frequency, for $j \in \widetilde{\mathcal{S}}_{\tilde{f}}^\gamma(m)$, as

$$\widetilde{\omega}_{\tilde{f}}(a_j, t_m) = \Im \left(\left(\widetilde{W}_{\tilde{f}}(a_j, t_m) \right)^{-1} \partial_b \widetilde{W}_{\tilde{f}}(a_j, t_m) \right),$$

with the time derivative of W_f estimated via (e.g., [10]):

$$\partial_b \widetilde{W}_{\tilde{f}}(a_j, \cdot) = \mathcal{F}_n^{-1} \left((\mathcal{F}_n \tilde{f}) \odot \widehat{\partial \psi}_j \right),$$

where $(\widehat{\partial \psi}_j)_m = a_j^{1/2} i \xi_m \widehat{\psi}(a_j \xi_m) / \Delta t$ for $m = 0, \dots, n-1$.

Finally, we normalize $\widetilde{\omega}$ by 2π so that the dominant frequency estimate is α when $f(t) = \cos(2\pi\alpha t)$.

C. Fast estimation of T_f from $\widetilde{W}_{\tilde{f}}$ and $\tilde{\omega}_{\tilde{f}}$

The representation $\widetilde{W}_{\tilde{f}}$ is given with respect to $n_a = Ln_v$ log-scale samples of the scale a , and this leads to several important considerations when estimating T_f via (3) and (4). First, due to lower resolutions in coarser scales, we expect to get lower resolutions in the lower frequencies. We thus divide the frequency domain into n_a components on a log scale. Second, sums with respect to a on a log scale, $a(z) = 2^{z/n_v}$ with $da(z) = a^{\frac{\log 2}{n_v}} dz$, lead to the modified integrand $W_f(a, b)a^{-1/2} \frac{\log 2}{n_v} dz$ in (4).

To choose the frequency divisions, note that the discretization period Δt limits the maximum frequency \bar{w} that can be estimated. The Nyquist theorem suggests that this frequency is $\bar{w} = w_{n_a-1} = \frac{1}{2\Delta t}$. Further, if we assume periodicity, the maximum period of an input signal is $n\Delta t$; thus the minimum frequency is $\underline{w} = w_0 = \frac{1}{n\Delta t}$. Combining these limits with the log scaling of the w 's we get the divisions: $w_l = 2^{l\Delta w} \underline{w}$, $l = 0, \dots, n_a - 1$, where $\Delta w = \frac{1}{n_a-1} \log_2(n/2)$. Note, the voice number n_v has a big effect on the frequency resolution.

We can now calculate the Synchrosqueezed estimate $\tilde{T}_{\tilde{f}}$. Our fast implementation of (4) finds the associated \mathcal{W}_l for each (a_j, t_m) and adds it to the correct sum, instead of performing a search over all scales for each l . This is possible because $\tilde{\omega}_{\tilde{f}}(a_j, t_m)$ only ever lands in one frequency bin. We provide pseudocode for this $O(n_a)$ implementation in Alg. 1.

Algorithm 1 Fast calculation of $\tilde{T}_{\tilde{f}}$ for fixed m

```

for  $l = 0$  to  $n_a - 1$  do {Initialize  $\tilde{T}$  for this  $m$ }
     $\tilde{T}_{\tilde{f}}(w_l, t_m) \leftarrow 0$ 
end for
for all  $j \in \tilde{\mathcal{S}}_f^\gamma(m)$  do {Calculate (4)}
    {Find frequency bin via  $w_l = 2^{l\Delta w} \underline{w}$ , and  $\tilde{\omega}_{\tilde{f}} \in \mathcal{W}_l$ }
     $l \leftarrow \text{ROUND} \left[ \frac{1}{\Delta w} \log_2 \left( \frac{\tilde{\omega}_{\tilde{f}}(a_j, b_m)}{\underline{w}} \right) \right]$ 
    if  $l \in [0, n_a - 1]$  then
        {Add normalized term to appropriate integral;  $\Delta z = 1$ }
         $\tilde{T}_{\tilde{f}}(w_l, t_m) \leftarrow \tilde{T}_{\tilde{f}}(w_l, t_m) + \frac{\log 2}{n_v} \widetilde{W}_{\tilde{f}}(a_j, t_m) a_j^{-1/2}$ 
    end if
end for

```

D. IF Curve Extraction and Filtered Reconstruction

A variety of signals, especially sums of quasi-harmonic signals with well-separated IFs, will have a frequency image $|T_f(w, b)|$ composed of several curves in the (w, b) plane. The image of the k th curve corresponds to both the IF $\phi'_k(b)$, and the entire component $A_k(b) \cos(\phi_k(b))$.

To extract a discretized curve c^* we maximize a functional of the energy of the curve that penalizes variation²:

$$\max_{c \in \{w_l\}^n} \sum_{m=0}^{n-1} E_{\tilde{T}}(w_{c_m}, t_m) - \lambda \sum_{m=1}^{n-1} \Delta w |c_m - c_{m-1}|^2, \quad (8)$$

where $E_{\tilde{T}}(w_l, t_m) = \log(|\tilde{T}_{\tilde{f}}(w_l, t_m)|^2)$ is the normalized energy of \tilde{T} . The user-defined parameter $\lambda > 0$ determines the “smoothness” of the resulting curve estimate (we use $\lambda = 10^5$). Its associated component \tilde{f}^* can be reconstructed via (5), by restricting the sum over l , at each t_m , to the neighborhood $\mathcal{N}_m = [c_m^* - n_w, c_m^* + n_w]$ (we use the window size $n_w = n_v/2$). The next curve is extracted by setting $\tilde{T}_{\tilde{f}}(\mathcal{N}_m, t_m) = 0$ for all m and repeating the process above.

IV. CONSISTENCY AND STABILITY OF SYNCHROSQUEEZING

We first review the main theorem on wavelet-based Synchronosqueezing, as developed in [5] (Thm. IV.1). Then we show that the components extracted via Synchronosqueezing are stable to bounded perturbations such as noise and discretization error.

We specify a class of functions on which these results hold. In practice, Synchronosqueezing works on a wider function class.

Definition IV.1 (Sums of Intrinsic Mode Type (IMT) Functions). The space $\mathcal{A}_{\epsilon, d}$ of superpositions of IMT functions, with smoothness ϵ and separation d , consists of functions having the form $f(t) = \sum_{k=1}^K f_k(t)$ with $f_k(t) = A_k(t)e^{i\phi_k(t)}$. For $t \in \mathbb{R}$ the IF components ϕ'_k are ordered and relatively well separated (high frequency components are spaced further apart than low frequency ones):

$$\forall t \quad \phi'_k(t) > \phi'_{k-1}(t), \quad \text{and}$$

$$\inf_t \phi'_k(t) - \sup_t \phi'_{k-1}(t) \geq d(\inf_t \phi'_k(t) + \sup_t \phi'_{k-1}(t)).$$

²The implementation of this step in the Synchronosqueezing Toolbox is a heuristic (greedy) approach that maximizes the objective at each time index, assuming the objective has been maximized for all previous time indices.

Functions in the class $\mathcal{A}_{\epsilon,d}$ are essentially composed of components with time-varying amplitudes. Furthermore, the amplitudes vary slowly, and the individual IFs are sufficiently smooth. For each k ,

$$A_k \in L^\infty \cap C^1, \quad \phi_k \in C^2, \quad \phi'_k, \phi''_k \in L^\infty, \quad \phi'_k(t) > 0,$$

$$\|A'_k\|_{L^\infty} \leq \epsilon \|\phi'_k\|_{L^\infty}, \quad \text{and} \quad \|\phi''_k\|_{L^\infty} \leq \epsilon \|\phi'_k\|_{L^\infty}.$$

For the theoretical analysis, we also define the Continuous Wavelet Synchrosqueezing transform, a smooth version of T_f .

Definition IV.2 (Continuous Wavelet Synchrosqueezing). Let $h \in C_0^\infty$ be a smooth function such that $\|h\|_{L^1} = 1$. The Continuous Wavelet Synchrosqueezing transform of function f , with accuracy δ and thresholds ϵ and M , is defined by

$$S_{f,\epsilon}^{\delta,M}(b, \eta) = \int_{\Gamma_{f,\epsilon}^{\delta,M}} \frac{W_f(a, b)}{a^{3/2}} \delta^{-1} h\left(\frac{|\eta - \omega_f(a, b)|}{\delta}\right) da \quad (9)$$

where $\Gamma_{f,\epsilon}^M = \{(a, b) : a \in [M^{-1}, M], |W_f(a, b)| > \epsilon\}$. We also denote $S_{f,\epsilon}^\delta = S_{f,\epsilon}^{\delta,\infty}$ and $\Gamma_{f,\epsilon}^\infty = \Gamma_{f,\epsilon}$, where the condition $a \in [M^{-1}, M]$ is replaced by $a > 0$.

The continuous (S_f^δ) and discrete frequency (T_f) Synchrosqueezing transforms are equivalent for small δ and large n_v , respectively. The frequency term η in (9) is equivalent to w_l in (4), and the integrand term $\frac{1}{\delta} h(\frac{\cdot}{\delta})$ in (9) takes the place of constraining the frequencies to \mathcal{W}_l in (4). Signal reconstruction and filtering analogues via the continuous Synchrosqueezing transform thus reduce to integrating $S_{f,\epsilon}^\delta$ over $\eta > 0$, similar to summing over l in (5).

The following consistency theorem was proved in [5]:

Theorem IV.1 (Synchrosqueezing Consistency). *Suppose $f \in \mathcal{A}_{\epsilon,d}$. Pick a wavelet $\psi \in C^1$ such that its Fourier transform $\widehat{\psi}(\xi)$ is supported in $[1 - \Delta, 1 + \Delta]$ for some $\Delta < \frac{d}{1+d}$. Then for sufficiently small ϵ , Synchrosqueezing can identify and extract the components $\{f_k\}$ from f :*

1. The Synchrosqueezing plot $|S_f^\delta|$ is concentrated around the IF curves $\{\phi'_k\}$. For each k , define the “scale band” $Z_k = \{(a, b) : |a\phi'_k(b) - 1| < \Delta\}$. For sufficiently small ϵ , the FM-demodulated frequency estimate ω_f is accurate inside Z_k where W_f is sufficiently large ($|W_f(a, b)| > \epsilon^{1/3}$):

$$|\omega_f(a, b) - \phi'_k(b)| \leq \epsilon^{1/3}.$$

Outside the scale bands $\{Z_k\}$, W_f is small:

$$|W_f(a, b)| \leq \epsilon^{1/3}.$$

2. Each component f_k may be reconstructed by integrating S_f^δ over a neighborhood around ϕ'_k . Choose the Wavelet threshold $\epsilon^{1/3}$ and let $N_k(b) = \{\eta : |\eta - \phi'_k(b)| \leq \epsilon^{1/3}\}$. For sufficiently small ϵ , there is a constant C_1 such that for all $b \in \mathbb{R}$,

$$\left| \lim_{\delta \rightarrow 0} \left(\mathcal{R}_\psi^{-1} \int_{N_k(b)} S_{f, \epsilon^{1/3}}^\delta(b, \eta) d\eta \right) - f_k(b) \right| \leq C_1 \epsilon^{1/3}.$$

Note that, as expected, Thm. IV.1 implies that components f_k with low amplitude may be difficult to identify and extract (as their Wavelet magnitudes may fall below $\epsilon^{1/3}$).

Thm. IV.1 also applies to discrete Synchronosqueezing, with the following modifications: letting $\delta \rightarrow 0$ is equivalent to letting $n_v \rightarrow \infty$. For reconstruction via (5), the integral over η should be replaced by a sum over l in the discrete neighborhood $N_k(b) = \{l : |w_l - \phi'_k(b)| \leq \epsilon^{1/3}\}$. Finally, the threshold $\epsilon^{1/3}$ in Thm. IV.1 part 2 can be applied numerically by letting $\gamma > \epsilon^{1/3}$ when calculating the discrete support S_f^γ .

We are now ready to state our main theorem:

Theorem IV.2 (Synchronosqueezing stability to small perturbations). *The statements in Thm. IV.1 essentially still hold if f is corrupted by a small error e , especially for mid-range IFs.*

Let $f \in \mathcal{A}_{\epsilon, d}$ and suppose we have a corresponding ϵ , h , ψ , Δ , and Z_k as given in Thm. IV.1. Furthermore, assume that $g = f + e$, where e is a bounded perturbation such that $\|e\|_{L^\infty} \leq C_\psi \epsilon$, where $C_\psi^{-1} = \max(\|\psi\|_{L^1}, \|\psi'\|_{L^1})$. For each k define the ‘‘maximal frequency range’’ $M_k \geq 1$ such that $\phi'_k(t) \in [M^{-1}, M]$ for all t . A mid-range IF is defined as having M_k near 1.

1. The Synchronosqueezing plot $|S_g^\delta|$ is concentrated around the IF curves $\{\phi'_k\}$. For sufficiently small ϵ , the FM-demodulated frequency estimate ω_g is accurate inside Z_k where W_g is sufficiently large ($|W_g(a, b)| > M_k^{1/2} \epsilon + \epsilon^{1/3}$):

$$|\omega_g(a, b) - \phi'_k(b)| \leq C_2 \epsilon^{1/3},$$

where $C_2 = O(M_k)$. Outside the scale bands $\{Z_k\}$, W_g is small:

$$|W_g(a, b)| \leq M_k^{1/2} \epsilon + \epsilon^{1/3}.$$

2. Each component f_k may be reconstructed with accuracy proportional to the noise magnitude and its maximal frequency range by integrating S_g^δ over a neighborhood around ϕ'_k . Choose the wavelet threshold $M_k^{1/2} \epsilon^{1/3} + \epsilon$ and let $N'_k(b) = \{\eta : |\eta - \phi'_k(b)| \leq C_2 \epsilon^{1/3}\}$, where (as before) $C_2 = O(M_k)$.

For sufficiently small ϵ ,

$$\left| \lim_{\delta \rightarrow 0} \left(\mathcal{R}_\psi^{-1} \int_{N'_k(b)} S_{g, M_k^{1/2} \epsilon + \epsilon^{1/3}}^{\delta, M_k}(b, \eta) d\eta \right) - f_k(b) \right| \leq C_3 \epsilon^{1/3},$$

where $C_3 = O(M_k)$.

The proof of Thm. IV.2 is deferred to §B.

Thm. IV.2 has two important implications. First, components with mid-range IF tend to have the best estimates and lowest reconstruction error under bounded noise. Second, to best identify signal component f_k with IF $\phi'_k \in [M^{-1}, M]$, from a noisy signal, the threshold γ should be chosen proportional to $M^{1/2}\epsilon$, where ϵ is an estimate of the noise magnitude.

A. Stability under Spline Interpolation

In many applications, samples of a signal $f \in \mathcal{A}$ are only given at irregular sample points $\{t'_m\}$, and these are spline interpolated to a function f_s . Thm. IV.2 bounds the error incurred due to this preprocessing:

Corollary IV.3. *Let $D = \max_m |t'_{m+1} - t'_m|$ and let $e = f_s - f$. Then the error in the estimate of the k th IF of T_{f_s} is $O(M_k D^{4/3})$, and the error in extracting f_k is $O(M_k D^{4/3})$.*

Proof: This follows from Thm. IV.2 and the following standard estimate on cubic spline approximations [11, p. 97]:

$$\|e\|_{L^\infty} \leq \frac{5}{384} D^4 \|f^{(4)}\|_{L^\infty}.$$

■

Thus, we can Synchronosqueeze f_s instead of f and, as long as the minimum sampling rate D^{-1} is high enough, the results will match. Furthermore, in practice errors are localized in time to areas of low sampling rate, low component amplitude, and/or high component frequency (see, e.g., §V).

V. EXAMPLES OF SYNCHROSQUEEZING PROPERTIES

We now provide numerical examples of several important properties of Synchronosqueezing. First, we compare Synchronosqueezing with two common analysis transforms.

A. Comparison of Synchrosqueezing to the CWT and STFT

We compare Synchrosqueezing to the Wavelet transform and the Short Time Fourier Transform (STFT) [12]. We show its superior precision, in both time and frequency, at identifying components of sums of quasi-harmonic signals.

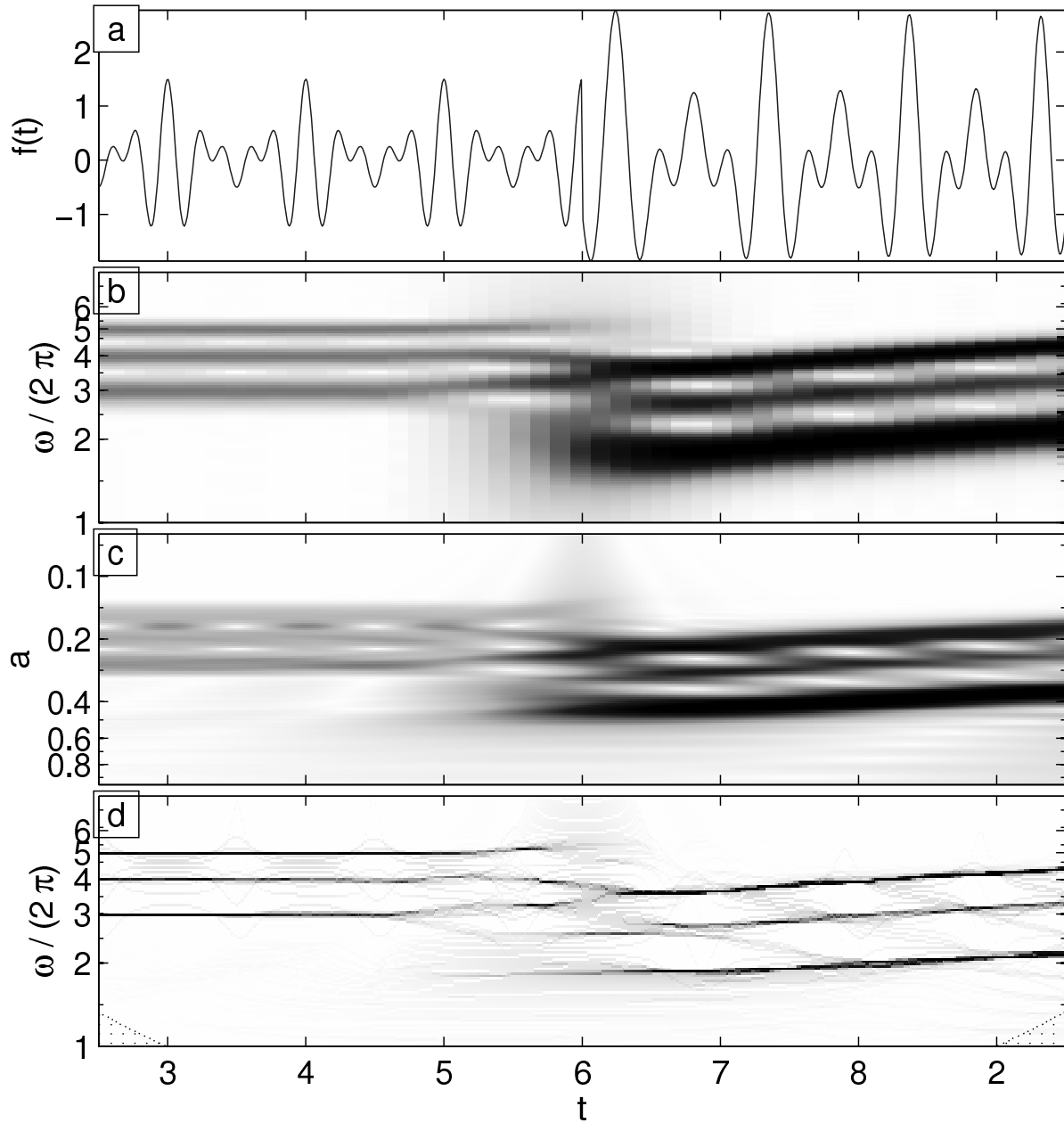


Fig. 2. Comparison of Synchrosqueezing with Wavelet and the STFT. (a) Synthetic signal $s(t)$. (b) Short Time Fourier Transformed signal. (c) Wavelet transformed: $W_s(a, t)$. (d) Synchrosqueezed: $T_s(\omega, t)$.

In Fig. 2 we focus on a signal $s(t)$ defined on $t \in [0, 10]$, that contains an abrupt transition at $t = 5$, and time-varying AM and FM modulation. It is discretized to $n = 1024$ points and is composed of the following components:

$$\begin{aligned}
 t < 5 : s_1(t) &= .5 \cos(2\pi(3t)), s_2(t) = .5 \cos(2\pi(4t)), \\
 s_3(t) &= .5 \cos(2\pi(5t)) \\
 t \geq 5 : s_1(t) &= \cos(2\pi(.5t^{1.5})), \\
 s_2(t) &= \exp(-t/20) \cos(2\pi(.75t^{1.5})), \\
 s_3(t) &= \cos(2\pi t^{1.5}).
 \end{aligned}$$

We used the shifted bump wavelet (see §A) and $n_v = 32$ for both the Wavelet and Synchronsqueezing transforms, and a Hamming window with length 300 and overlap of length 285 for the STFT. These STFT parameters focused on optimal precision in frequency, but not in time [12]. For $t < 5$, the harmonic components of $s(t)$ are clearly identified in the Synchronsqueezing plot T_s (Fig. 2(d)) and the STFT plot (Fig. 2(b)), though the frequency estimate is more precise in T_s . The higher frequency components are better estimated up to the singularity at $t = 5$ in T_s , but in the STFT there is mixing at the singularity. For $t \geq 5$, the frequency components are more clearly visible in T_s due to the smearing of lower frequencies in the STFT. The temporal resolution in the STFT is also significantly lower than for Synchronsqueezing due to the selected parameters. A shorter window in the STFT will provide higher temporal resolution, but lower frequency resolution and more smearing between the three components.

B. Nonuniform Sampling and Splines

We now demonstrate how Synchronsqueezing and extraction work for a more complicated signal that contains multiple time-varying amplitude and frequency components, and has been irregularly subsampled. Let

$$\begin{aligned}
 f(t) &= \cos(4\pi t) \\
 &+ (1 + 0.2 \cos(2.5t)) \cos(2\pi(5t + 2t^{1.2})) \\
 &+ e^{-0.2t} \cos(2\pi(3t + 0.2 \cos(t))),
 \end{aligned} \tag{10}$$

and let the sampling times be perturbations of uniformly spaced times having the form $t'_m = \Delta t_1 m + \Delta t_2 u_m$, where $\Delta t_2 < \Delta t_1$ and $\{u_m\}$ is sampled from the uniform distribution on $[0, 1]$. Here we fix $\Delta t_1 = 11/180$ and $\Delta t_2 = 11/600$. This leads to ≈ 160 samples on the interval $t \in [0, 10]$. To correct

for nonuniform sampling, we fit a spline through $(t'_m, f(t'_m))$ to get the function $f_s(t)$ and discretize on the finer grid $t_m = m\Delta t$, with $\Delta t = 10/1024$ and $m = 0, \dots, 1023$. The resulting vector, \tilde{f}_s , is a discretization of the original signal plus a spline error term. Fig. 3(a) shows \tilde{f}_s for $t \in [2, 8]$.

Figs. 3(b-e) show the results of Synchrosqueezing and component extraction of \tilde{f}_s , for $t \in [2, 8]$. All three components are well separated in the TF domain. The second component is the most difficult to reconstruct, as it contains the highest frequency information. Due to stability (Thm. IV.2 and Cor. IV.3), extraction of components with mid-range IFs is more stable to the error $e(t)$. Fig. 3 shows that reconstruction errors are time localized to the locations of errors in \tilde{f}_s .

C. White Noise and Reconstruction

We take the signal $f(t)$ of (10), now regularly sampled on the fine grid with $\Delta t = 10/1024$ ($n = 1024$ samples) as before, and corrupt it with white Gaussian noise having a standard deviation of $\sigma_N = 1.33$. This signal, \tilde{f}_N (see Fig. 4(a)) has an SNR of -1 dB.

Figs. 4(b-e) show the results of Synchrosqueezing and component extraction of \tilde{f}_N , for $t \in [2, 8]$. As seen in Fig. 4(b), most of the additional energy, caused by the white noise, appears in the higher frequencies. Again, all three components are well separated in the TF domain, though now the third, lower-amplitude, component experiences a “split” at $t \approx 6.5$. Reconstruction of signal components is less reliable in locations of high frequencies and low magnitudes (note the axis in Fig. 4(e) is half that of the others). This again numerically confirms Thm. IV.2: components with mid-range IFs and higher amplitudes are more stable to the noise.

VI. ASPECTS OF THE MID-PLEISTOCENE TRANSITION

In this section we apply Synchrosqueezing to analyze the characteristics of a calculated index of the incoming solar radiation (insolation) and to measurements of repeated transitions between glacial (cold) and interglacial (warm) climates during the Pleistocene epoch: ≈ 1.8 Myr to 12 kyr before the present.

The Earth’s climate is a complex, multi-component nonlinear, system with significant stochastic elements [13]. The key external forcing field is the insolation at the top of the atmosphere (TOA). Local insolation has predominately harmonic characteristics in time (diurnal cycle, annual cycle and Milanković orbital cycles). However, response of planetary climate, which varies at all time scales [14], also depends on random perturbations (e.g., volcanism), solid boundary conditions (e.g., plate tectonics and global ice distribution), internal variability and feedbacks (e.g., global carbon cycle). Various paleoclimate records or proxies provide us with information about past climates beyond observational records. Proxies are

biogeochemical tracers, i.e., molecular or isotopic properties, imprinted into various types of deposits (e.g., deep-sea sediment), and they indirectly represent physical conditions (e.g., temperature) at the time of deposition. We focus on climate variability during the last 2.5 Myr (that also includes the late Pliocene) as recorded by $\delta^{18}O$ in foraminiferal shells at the bottom of the ocean (benthic forams). Benthic $\delta^{18}O$ is the deviation of the ratio of ^{18}O to ^{16}O in sea water with respect to the present-day standard, as imprinted in benthic forams during their growth. It increases with glaciation during cold climates because ^{16}O evaporates more readily and accumulates in ice sheets. Thus, benthic $\delta^{18}O$ can be interpreted as a proxy for either high-latitude temperature or global ice volume.

We first examine a calculated element of the TOA solar forcing field. Fig. 5(a) shows f_{SF} , the mid-June insolation at $65^\circ N$ at 1 kyr intervals [15]. This TOA forcing index does not encompass the full complexity of solar radiation structure and variability, but is commonly used to gain insight into the timing of advances and retreats of ice sheets in the Northern Hemisphere in this period (e.g., [16]). The Wavelet and Synchrosqueezing decompositions in Fig. 6(a) and Fig. 7(a), respectively, show the key harmonic components of f_{SF} . The application of a shifted bump mother wavelet (see §A) yields an upward shift of the spectral features along the scale axis in each of the the representations in Fig. 6. Therefore the scale a should not be used to directly infer periodicities. In contrast, the Synchrosqueezing spectrums in Fig. 7 explicitly present time-frequency (or here specifically time-periodicity) decompositions with a sharper structure, and are not affected by the scale shift inherent in the choice of mother wavelet.

Fig. 7(a) clearly shows the presence of strong precession cycles (at periodicities $\tau=19$ kyr and 23 kyr), obliquity cycles (primary at 41 kyr and secondary at 54 kyr), and very weak eccentricity cycles (primary periodicities at 95 kyr and 124 kyr, and secondary at 400 kyr). This is in contrast with Fig. 6(a), which contains blurred and shifted spectral structures only qualitatively similar to Fig. 7(a).

We next analyze the climate response during the last 2.5 Myr as deposited in benthic $\delta^{18}O$ in long sediments cores. Fig. 5(b) shows f_{CR1} : benthic $\delta^{18}O$, sampled at irregular time intervals from a single core, DSDP Site 607, in the North Atlantic [17]. This signal was spline interpolated to 1 kyr intervals prior to the spectral analyses. Fig. 5(c) shows f_{CR2} : the benthic $\delta^{18}O$ stack (H07) calculated at 1 kyr intervals from fourteen cores (most of them from the Northern Hemisphere, including DSDP607) using the extended depth-derived age model [18]. Prior to combining the cores in the H07 stack, the record mean between 0.7 Myr ago and the present was subtracted from each $\delta^{18}O$ record; this is the cause of the differing vertical ranges in Figs. 5(b-c). Noise due to local climate characteristics and measurement errors of each core is reduced when we shift the spectral analysis from DSDP607 to the stack; and this is particularly visible in the finer scales and higher frequencies. The Synchrosqueezing decomposition

in Fig. 7(c) is a more precise time-frequency representation of the stack than a careful STFT analysis [18, Fig. 4]. In addition, it shows far less stochasticity above the obliquity band as compared to Fig. 7(b), enabling the 23 kyr precession cycle to become mostly coherent over the last 1 Myr. Thanks to the stability of Synchronosqueezing, the spectral differences below the obliquity band are less pronounced between Fig. 7(b) and Fig. 7(c). Overall, the stack reveals sharper time-periodicity evolution of the climate system than DSDP607 or any other single core possibly could. The Wavelet representations in Figs. 6(b-c) also show this suppression of noise in the stack (in more diffuse and scale shifted patterns). The time average of Synchronosqueezing magnitudes (normalized by $1/R_\psi$) is directly comparable with the Fourier spectrum, but delineates the harmonic components much more clearly (not shown).

During the last 2.5 Myr, the Earth experienced a gradual decrease in global background temperature and CO₂ concentration, and an increase in mean global ice volume accompanied with glacial-interglacial oscillations that have intensified towards the present (this is evident in Fig. 5(b) and 5(c)). The mid-Pleistocene transition, occurring gradually or abruptly sometimes between 1.2 Myr and 0.6 Myr ago, was the shift from 41 kyr-dominated glacial cycles to 100 kyr-dominated glacial cycles recorded in deep-sea proxies (e.g., [19]–[21]). The origin of this strong 100 kyr cycle in the late-Pleistocene climate and the prior incoherency of the precession band are still unresolved questions. Both types of spectral analyses of selected $\delta^{18}O$ records indicate that the climate system does not respond linearly to external periodic forcing.

Synchronosqueezing enables the detailed time-frequency decomposition of a noisy, nonstationary, climate time series due to stability (Thm. IV.2) and more precisely reveals key modulated signals that rise above the stochastic background. The gain (the ratio of the climate response amplitude to insolation forcing amplitude) at a given frequency or period, is not constant. The response to the 41 kyr obliquity cycle is present almost throughout the entire Pleistocene in Fig. 7(c). The temporary incoherency of the 41 kyr component starting about 1.25 Myr ago roughly coincides with the initiation of a lower frequency signal (≈ 70 kyr) that evolves into a strong 100 kyr component in the late Pleistocene (about 0.6 Myr ago). Inversion (e.g., spectral integration) of the Synchronosqueezing decomposition of f_{SF} and f_{CR2} across the key orbital frequency bands in Fig. 8 again emphasize the nonlinear relation between insolation and climate evolution. Specifically, in Fig. 8(a) the amplitude of the filtered precession signal of f_{CR2} abruptly rises 1 Myr ago, while in Fig. 8(c) the amplitude of the eccentricity signal shows a gradual increase.

Synchronosqueezing analysis of the solar insolation index and benthic $\delta^{18}O$ makes a significant contribution in three important ways. First, it produces spectrally sharp traces of complex system evolution through the high-dimensional climate state space (compare with, e.g., [20, Fig. 2]). Second, it delineates

the effects of noise on specific frequency ranges when comparing a single core to the stack. Low frequency components are mostly robust to noise induced by both local climate variability and the measurement process. Third, thanks to its precision, Synchrosqueezing allows the filtered reconstruction of signal components within frequency bands.

Questions about the key physical processes governing large scale climate variability over the last 2.5 Myr can be answered with sufficient accuracy only by precise data analysis and the development of a hierarchy of models at various levels of complexity that reproduce the key aspects of Pleistocene history. The resulting dynamic stochastic understanding of past climates may benefit predictions of future climates.

VII. CONCLUSIONS AND FUTURE WORK

Synchrosqueezing can be used to extract the instantaneous spectra of, and filter, a wide variety of signals that include complex simulation data (e.g. dynamical models), and physical signals (e.g. climate proxies). A careful implementation runs in $O(n_v n \log^2 n)$ time, and is stable (in theory and in practice) to errors in these types of signals. We have shown how it can be used to help address an important problem in climatology.

Other areas in which the authors are using this tool include ECG analysis (respiration and T-end detection), meteorology and oceanography (large-scale teleconnection and ocean-atmosphere interaction). Additional future work includes theoretical analysis of the Synchrosqueezing transform.

APPENDIX A

INVARIANCE TO THE UNDERLYING TRANSFORM

As mentioned in §II and in [5], Synchrosqueezing is invariant to the underlying choice of transform. The only differences one sees in practice are due to two factors: the time compactness of the underlying analysis atom (e.g. mother wavelet), and the frequency compactness of this atom. That is, $|\psi(t)|$ should fall off quickly away from zero, $\widehat{\psi}(\xi)$ is ideally zero for $\xi < 0$, and Δ (of Thm. IV.1) is small.

Fig. 9 shows the effect of Synchrosqueezing the discretized spline signal \tilde{f}_s of the synthetic nonuniform sampling example in the main article, using three different complex CWT mother wavelets. These wavelets

are:

a. Morlet (shifted Gaussian)

$$\widehat{\psi}_a(\xi) \propto \exp(-(\mu - \xi)^2/2), \quad \xi \in \mathbb{R}$$

b. Complex Mexican Hat

$$\widehat{\psi}_b(\xi) \propto \xi^2 \exp(-\sigma^2 \xi^2/2), \quad \xi > 0$$

c. Shifted Bump

$$\widehat{\psi}_d(\xi) \propto \exp\left(-\left(1 - \left(\frac{\xi - \mu}{\sigma}\right)^2\right)^{-1}\right),$$

$$\xi \in [\sigma(\mu - 1), \sigma(\mu + 1)]$$

where for ψ_a we use $\mu = 2\pi$, for ψ_b we use $\sigma = 1$, for and for ψ_c we use $\mu = 5$ and $\sigma = 1$.

The Wavelet representations of \tilde{f}_s differ due to differing mother wavelets, but the Synchrosqueezing representation is mostly invariant to these differences. As expected from Thm. IV.1, more accurate representations are given by wavelets having compact frequency support on ξ away from 0.

APPENDIX B

SYNCHROSQUEEZING STABILITY: DEFERRED PROOF

We prove the stability theorem of §IV. Below, let $\tilde{\epsilon} = \epsilon^{1/3}$.

Proof of Thm. IV.2: Synchrosqueezing Stability: Using Hölder's inequality, it is clear that

$$|W_f(a, b) - W_g(a, b)| \leq \|f - g\|_{L^\infty} a^{1/2} \quad (11)$$

$$\times \int_{-\infty}^{\infty} \left| \psi\left(t - \frac{b}{a}\right) \right| dt \leq a^{1/2} \epsilon.$$

Similarly, we also have $|\partial_b W_f(a, b) - \partial_b W_g(a, b)| \leq a^{-1/2} \epsilon$. Now if $(a, b) \notin Z_k$ for any k , then using Thm. IV.1 gives

$$|W_g(a, b)| \leq |W_g(a, b) - W_f(a, b)| + |W_f(a, b)|$$

$$\leq M_k^{1/2} \epsilon + \tilde{\epsilon}. \quad (12)$$

On the other hand, if for some k , $(a, b) \in Z_k$ and $|W_g(a, b)| > M_k^{1/2}\epsilon + \tilde{\epsilon}$, then by (11) and Thm. IV.1,

$$\begin{aligned}
|\omega_g(a, b) - \phi'_k(b)| &\leq |\omega_g(a, b) - \omega_f(a, b)| + |\omega_f(a, b) - \phi'_k(b)| \\
&\leq \left| \frac{W_g(a, b) - W_f(a, b)}{W_g(a, b)W_f(a, b)} \partial_b W_f(a, b) \right. \\
&\quad \left. + \frac{\partial_b W_f(a, b) - \partial_b W_g(a, b)}{W_g(a, b)} \right| + \tilde{\epsilon} \\
&\leq \frac{M_k^{1/2}\epsilon}{(M_k^{1/2}\epsilon + \tilde{\epsilon})\tilde{\epsilon}} \left(M_k^{1/2} \|f\|_{L^\infty} \|\psi\|_{L^1} \right) \\
&\quad + \frac{M_k^{1/2}\epsilon}{M_k^{1/2}\epsilon + \tilde{\epsilon}} + \tilde{\epsilon} \\
&\leq C_2\tilde{\epsilon}
\end{aligned} \tag{13}$$

for some C_2 depending only on f , ψ and M_k . For the second part of Thm. IV.2, we fix k and b and use the following calculation (see [5, p.12]):

$$\begin{aligned}
\lim_{\delta \rightarrow 0} \int_{|\eta - \phi'_k(b)| \leq \tilde{\epsilon}} S_{f, \tilde{\epsilon}}^\delta(b, \eta) d\eta \\
= \int_{P(a, f, \tilde{\epsilon}, \tilde{\epsilon}, \infty)} a^{-3/2} W_f(a, b) da,
\end{aligned} \tag{14}$$

where $P(a, f, \epsilon_1, \epsilon_2, M) := \{a : |W_f(a, b)| > \epsilon_1, \omega_f(a, b) - \phi'_k(b)| \leq \epsilon_2, a \in [M^{-1}, M]\}$.

It is also shown in [5, p. 12] that if $a \in P(a, f, \tilde{\epsilon}, \tilde{\epsilon}, \infty)$, then $(a, b) \in Z_k$, so $M_k^{-1} \leq a \leq M_k$. This means that in (14), we can replace $S_{f, \tilde{\epsilon}}^\delta(b, \eta)$ by $S_{f, \tilde{\epsilon}}^{\delta, M_k}(b, \eta)$ and $P(a, f, \tilde{\epsilon}, \tilde{\epsilon}, \infty)$ by $P(a, f, \tilde{\epsilon}, \tilde{\epsilon}, M_k)$. We can also get a result identical to (14) for g by simply repeating the argument in [5]. First, note that as $\delta \rightarrow 0$, the expression

$$\int_{|\eta - \phi'_k(b)| \leq C_2\tilde{\epsilon}} a^{-3/2} W_g(a, b) \frac{1}{\delta} h \left(\frac{|\eta - \omega_g(a, b)|}{\delta} \right) d\eta \tag{15}$$

converges to $a^{-3/2} W_g(a, b) \chi_{\{|\omega_g(a, b) - \phi'_k(b)| < C_2\tilde{\epsilon}\}}(a)$ for almost all $a \in [M_k^{-1}, M_k]$. This shows that

$$\begin{aligned}
\lim_{\delta \rightarrow 0} \int_{|\eta - \phi'_k(b)| \leq C_2\tilde{\epsilon}} S_{g, M_k^{1/2}\epsilon + \tilde{\epsilon}}^{\delta, M_k}(b, \eta) d\eta \\
= \int_{(a, b) \in \Gamma_{g, M_k^{1/2}\epsilon + \tilde{\epsilon}}^{M_k}} \lim_{\delta \rightarrow 0} \int_{|\eta - \phi'_k(b)| \leq C_2\tilde{\epsilon}} \\
a^{-3/2} W_g(a, b) \frac{1}{\delta} h \left(\frac{|\eta - \omega_g(a, b)|}{\delta} \right) d\eta da
\end{aligned} \tag{16}$$

$$= \int_{P(a, g, M_k^{1/2}\epsilon + \tilde{\epsilon}, C_2\tilde{\epsilon}, M_k)} a^{-3/2} W_g(a, b) da. \tag{17}$$

We can justify exchanging the order of integrations and limits in (16) by the Fubini and dominated convergence theorems, since (15) is bounded by $|a^{-3/2}W_g(a, b)| \in L^1(\{a : |W_g(a, b)| > M_k^{1/2}\epsilon + \tilde{\epsilon}, a \in [M_k^{-1}, M_k]\})$ for all δ . We also note that (11) and (13) show that in the set $P(a, f, \tilde{\epsilon}, \tilde{\epsilon}, M_k) \setminus P(a, g, M_k^{1/2}\epsilon + \tilde{\epsilon}, C_2\tilde{\epsilon}, M_k)$, we have $|W_f(a, b)| \leq 2M_k^{1/2}\epsilon + \tilde{\epsilon}$. We can now use the result of Thm. IV.1 along with (12), (14) and (17) to find that

$$\begin{aligned}
& \left| \lim_{\delta \rightarrow 0} \int_{|\eta - \phi'_k(b)| \leq \tilde{\epsilon}} S_{f, \tilde{\epsilon}}^{\delta, M_k}(b, \eta) d\eta - \right. \\
& \quad \left. \lim_{\delta \rightarrow 0} \int_{|\eta - \phi'_k(b)| \leq C_2\tilde{\epsilon}} S_{g, M_k^{1/2}\epsilon + \tilde{\epsilon}}^{\delta, M_k}(b, \eta) d\eta \right| \\
&= \left| \int_{P(a, f, \tilde{\epsilon}, \tilde{\epsilon}, M_k)} a^{-3/2} W_f(a, b) \right. \\
& \quad \left. - \int_{P(a, g, M_k^{1/2}\epsilon + \tilde{\epsilon}, C_2\tilde{\epsilon}, M_k)} a^{-3/2} W_g(a, b) da \right| \\
&\leq \int_{P(a, g, M_k^{1/2}\epsilon + \tilde{\epsilon}, C_2\tilde{\epsilon}, M_k)} \left| a^{-3/2} (W_f(a, b) - W_g(a, b)) \right| da \\
& \quad + \int_{P(a, f, \tilde{\epsilon}, \tilde{\epsilon}, M_k) \setminus P(a, g, M_k^{1/2}\epsilon + \tilde{\epsilon}, C_2\tilde{\epsilon}, M_k)} \left| a^{-3/2} W_f(a, b) \right| da \\
&\leq \int_{M_k^{-1}}^{M_k} a^{-1} \epsilon da + \int_{M_k^{-1}}^{M_k} a^{-3/2} (2M_k^{1/2}\epsilon + \tilde{\epsilon}) da \\
&\leq (2 \log M_k) \epsilon + 2 (M_k^{1/2} - M_k^{-1/2}) (2M_k^{1/2}\epsilon + \tilde{\epsilon}) \\
&\leq C_3 \tilde{\epsilon}.
\end{aligned}$$

Combining this with the result of Thm. IV.1 finishes the proof. ■

ACKNOWLEDGEMENT

The authors would like to thank Prof. Ingrid Daubechies for many insightful discussions. E. Brevdo acknowledges the NSF Graduate Research Fellowship grant No. DGE-0646086. N.S. Fučkar acknowledges valuable discussions with Prof. Axel Timmermann and Dr. Oliver Elison Timm. H.-T. Wu and G. Thakur acknowledge FHWA grant No. DTFH61-08-C-00028.

REFERENCES

- [1] P. Flandrin, *Time-frequency/time-scale analysis*, ser. Wavelet Analysis and its Applications. San Diego, CA: Academic Press Inc., 1999, vol. 10.
- [2] P. Flandrin, F. Auger, and E. Chassande-Mottin, “Time-Frequency Reassignment – From Principles to Algorithms,” in *Applications in time-frequency signal processing*, A. Papandreou-Suppappola, Ed. CRC, 2003.

- [3] S. Fulop and K. Fitz, “Algorithms for computing the time-corrected instantaneous frequency (reassigned) spectrogram, with applications,” *J. Acoust. Soc. Am.*, vol. 119, p. 360, 2006.
- [4] I. Daubechies and S. Maes, “A nonlinear squeezing of the continuous wavelet transform based on auditory nerve models,” *Wavelets in Medicine and Biology*, pp. 527–546, 1996.
- [5] I. Daubechies, J. Lu, and H.-T. Wu, “Synchrosqueezed wavelet transforms: An empirical mode decomposition-like tool,” *Applied and Computational Harmonic Analysis*, 2010.
- [6] N. Huang, Z. Shen, S. Long, M. Wu, H. Shih, Q. Zheng, N. Yen, C. Tung, and H. Liu, “The empirical mode decomposition and the Hilbert spectrum for nonlinear and non-stationary time series analysis,” *Proceedings: Mathematical, Physical and Engineering Sciences*, vol. 454, no. 1971, pp. 903–995, 1998.
- [7] I. Daubechies, *Ten lectures on wavelets*. Society for Industrial Mathematics, 1992.
- [8] G. Thakur and H. Wu, “Synchrosqueezing-based Recovery of Instantaneous Frequency from Nonuniform Samples,” *Submitted (Arxiv preprint arXiv:1006.2533)*, 2010.
- [9] P. Goupillaud, A. Grossmann, and J. Morlet, “Cycle-octave and related transforms in seismic signal analysis,” *Geoexploration*, vol. 23, no. 1, pp. 85–102, 1984.
- [10] E. Tadmor, “The exponential accuracy of Fourier and Chebyshev differencing methods,” *SIAM Journal on Numerical Analysis*, vol. 23, no. 1, pp. 1–10, 1986.
- [11] G. Stewart, *Afternotes goes to graduate school: lectures on advanced numerical analysis*. Society for Industrial Mathematics, 1998.
- [12] A. Oppenheim, R. Schaffer, and J. Buck, *Discrete-Time Signal Processing*. Prentice Hall, 1999.
- [13] R. Pierrehumbert, *Principles of planetary climate*. Cambridge University Press, 2010.
- [14] P. Huybers and W. Curry, “Links between annual, Milankovitch and continuum temperature variability,” *Nature*, vol. 441, no. 7091, pp. 329–332, 2006.
- [15] A. Berger and M. Loutre, “Astronomical solutions for paleoclimate studies over the last 3 million years,” *Earth and Planetary Science Letters*, vol. 111, no. 2-4, pp. 369–382, 1992.
- [16] J. Hays, J. Imbrie, N. Shackleton *et al.*, “Variations in the Earths orbit: pacemaker of the ice ages,” *Science*, vol. 194, no. 4270, pp. 1121–1132, 1976.
- [17] W. Ruddiman, M. Raymo, D. Martinson, B. Clement, and J. Backman, “Pleistocene evolution: northern hemisphere ice sheets and North Atlantic Ocean,” *Paleoceanography*, vol. 4, no. 4, pp. 353–412, 1989.
- [18] P. Huybers, “Glacial variability over the last two million years: an extended depth-derived agemodel, continuous obliquity pacing, and the Pleistocene progression,” *Quaternary Science Reviews*, vol. 26, no. 1-2, pp. 37–55, 2007.
- [19] W. Ruddiman, M. Raymo, and A. McIntyre, “Matuyama 41,000-year cycles: North Atlantic Ocean and northern hemisphere ice sheets,” *Earth and Planetary Science Letters*, vol. 80, no. 1-2, pp. 117–129, 1986.
- [20] P. Clark, D. Archer, D. Pollard, J. Blum, J. Rial, V. Brovkin, A. Mix, N. Piasias, and M. Roy, “The middle Pleistocene transition: characteristics, mechanisms, and implications for long-term changes in atmospheric pCO₂,” *Quaternary Science Reviews*, vol. 25, no. 23-24, pp. 3150–3184, 2006.
- [21] M. Raymo and P. Huybers, “Unlocking the mysteries of the ice ages,” *Nature*, vol. 451, no. 7176, pp. 284–285, 2008.

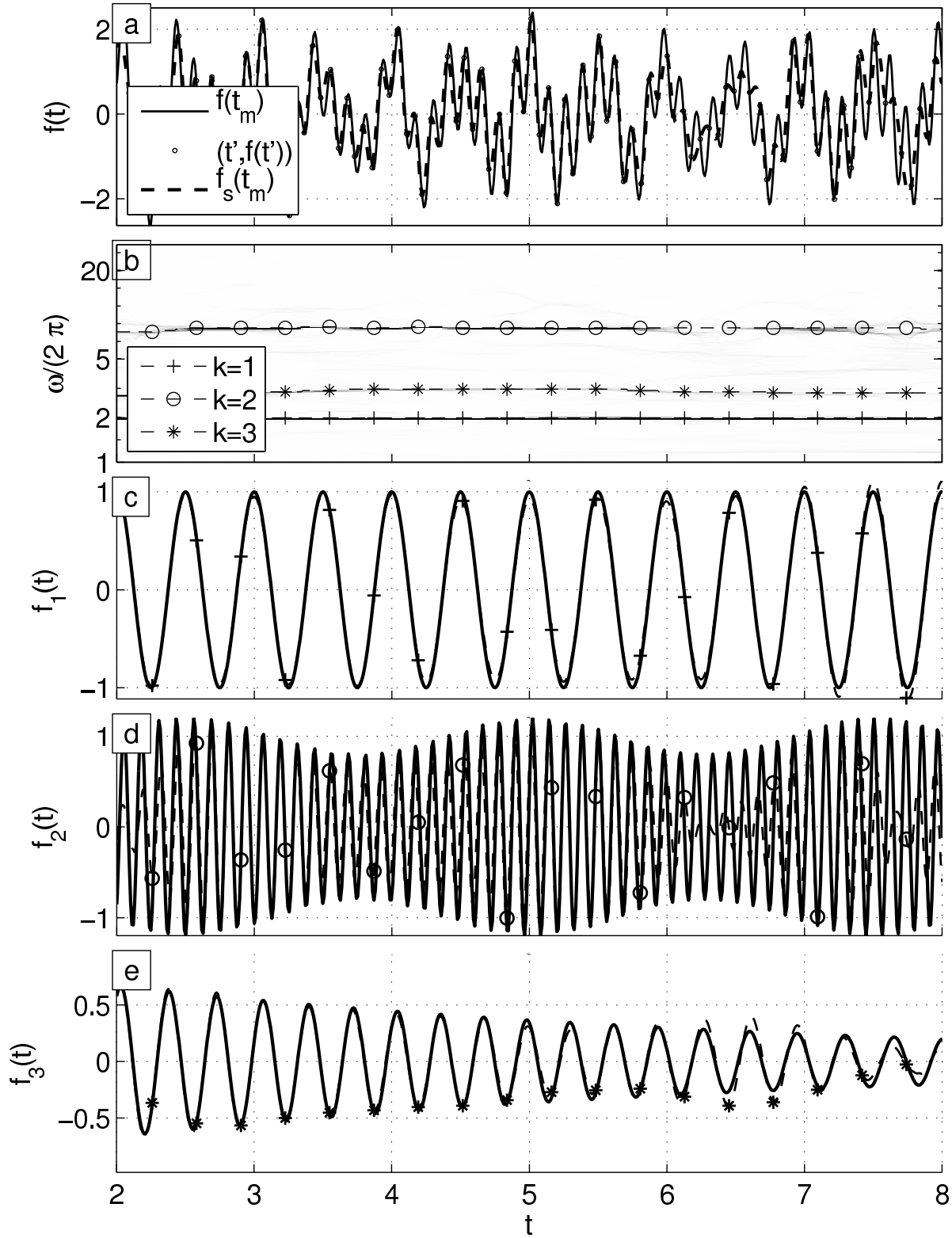


Fig. 3. (a) Nonuniform Sampling of f , with spline interpolation estimate \tilde{f}_s . (b) Synchrosqueezing $\tilde{T}_{\tilde{f}_s}$ of \tilde{f}_s ; components extracted via (8). (c-e) Extracted components \tilde{f}_k^* compared to originals \tilde{f}_k , $k = 1, 2, 3$ (respectively).

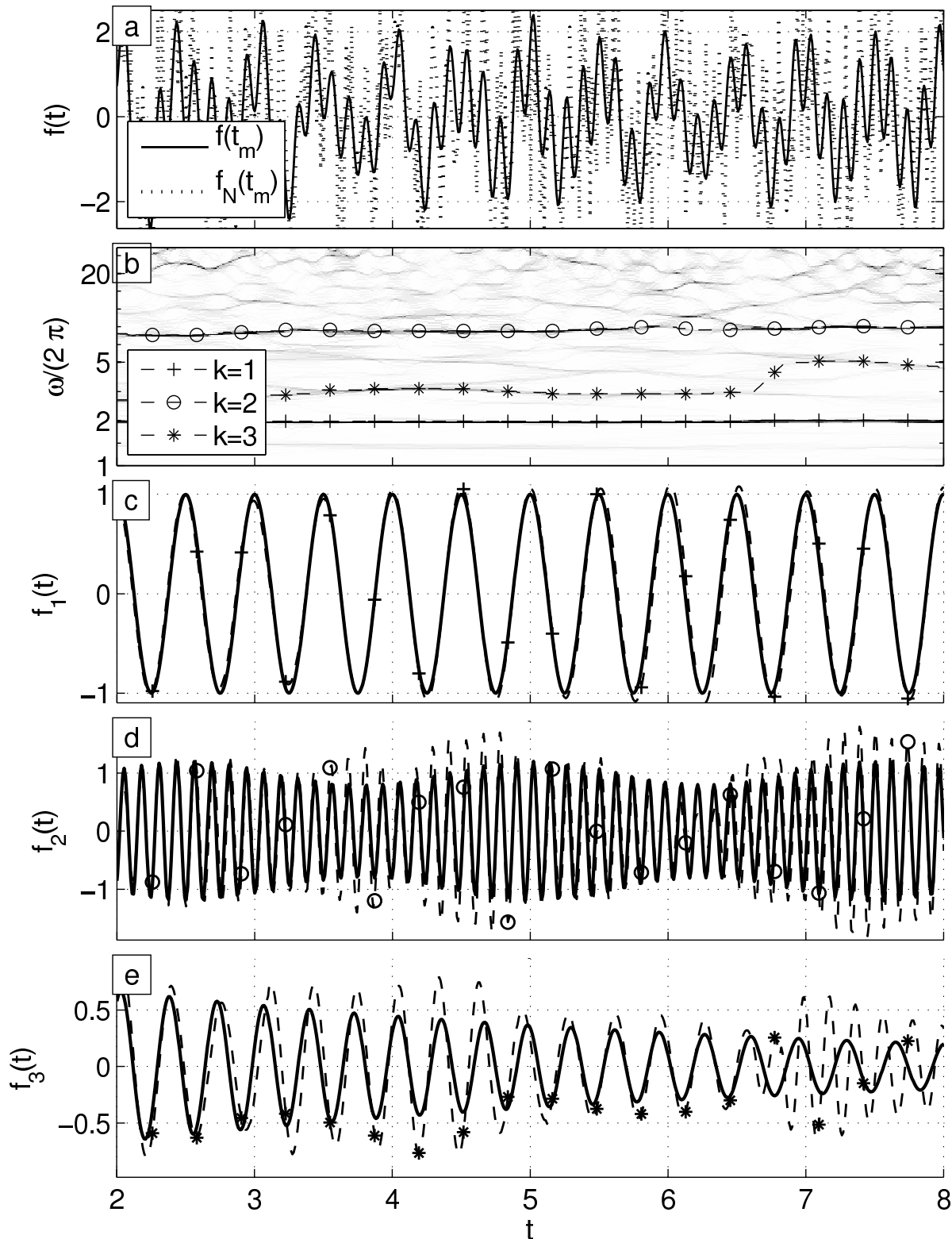


Fig. 4. (a) Uniform sampling of f , \tilde{f} , corrupted by normal white noise with standard deviation $\sigma_N = 1.33$ (SNR is -1 dB): \tilde{f}_N . (b) Synchrosqueezing $\tilde{T}_{\tilde{f}_N}$ of \tilde{f}_N ; components extracted via (8). (c-e) Extracted components \tilde{f}_k^* compared to originals \tilde{f}_k , $k = 1, 2, 3$ (respectively).

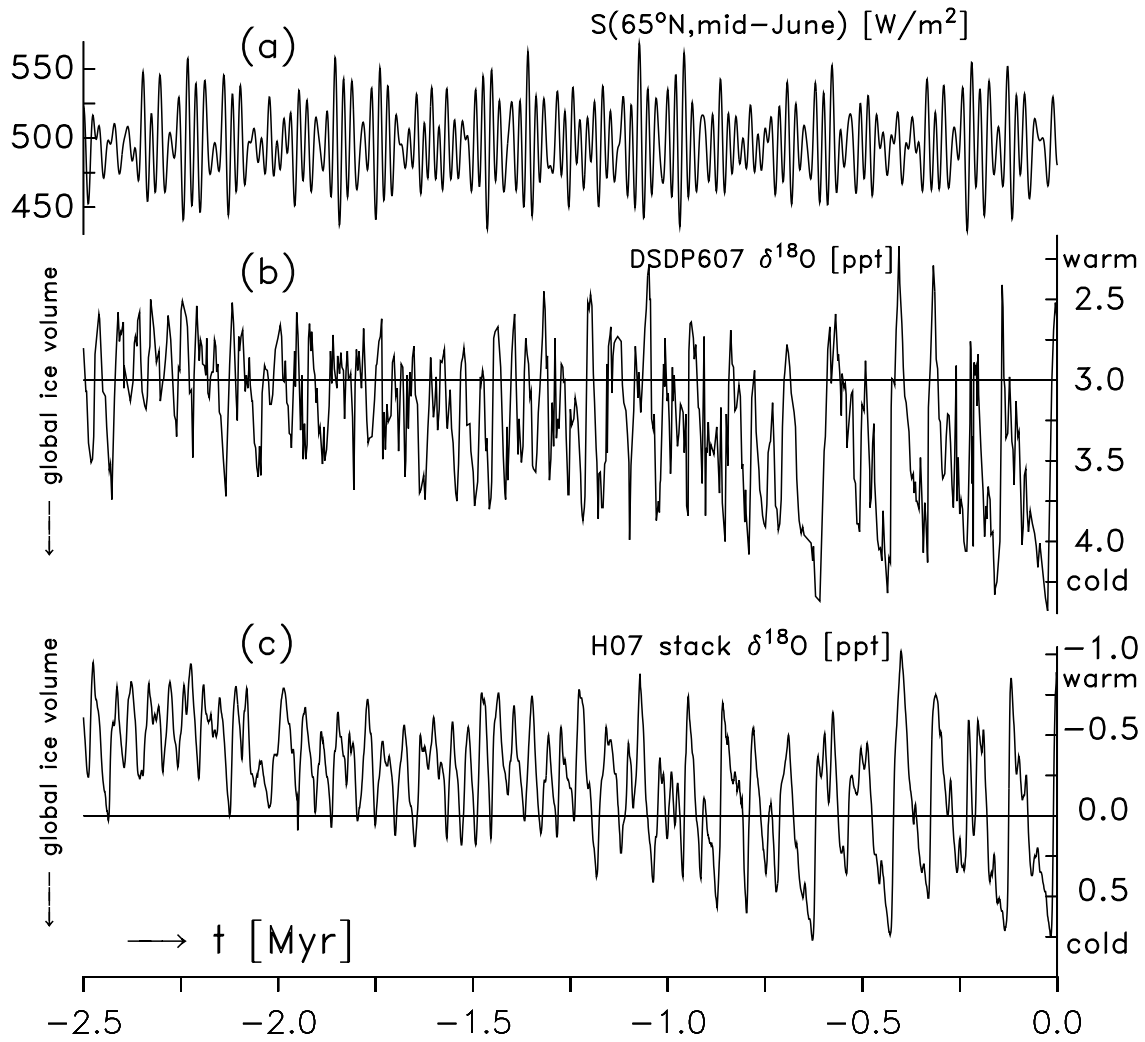


Fig. 5. (a) Calculated mid-June insolation flux at 65°N : f_{SF} . Climate response as recorded by benthic $\delta^{18}\text{O}$ (b) in DSDP607 core: f_{CR1} , and (c) in H07 stack: f_{CR2} .

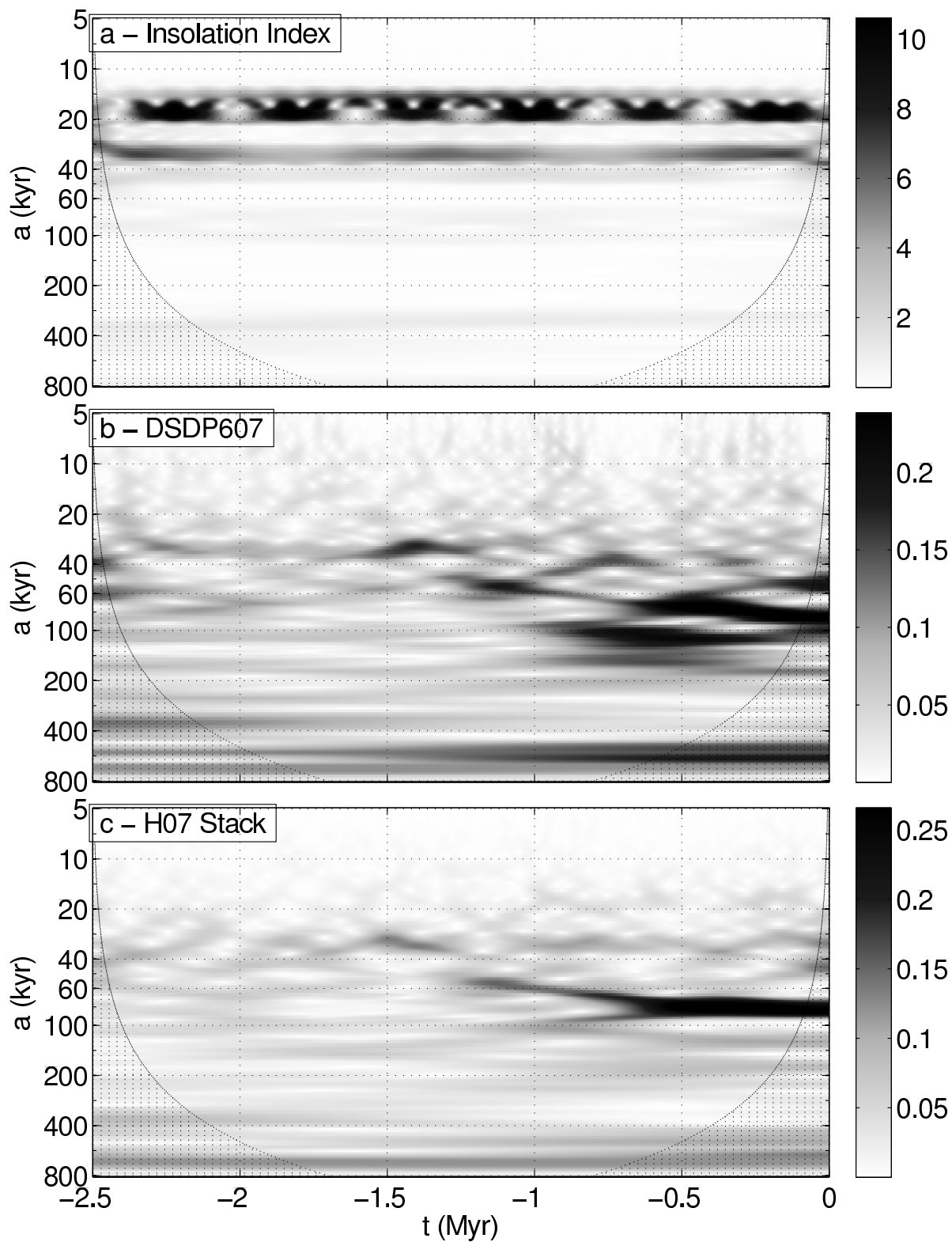


Fig. 6. Wavelet magnitude time evolution of (a) insolation index f_{SF} , and climate response in benthic $\delta^{18}O$ of (b) DSDP607 core, f_{CR1} , and (c) H07 stack, f_{CR2} .

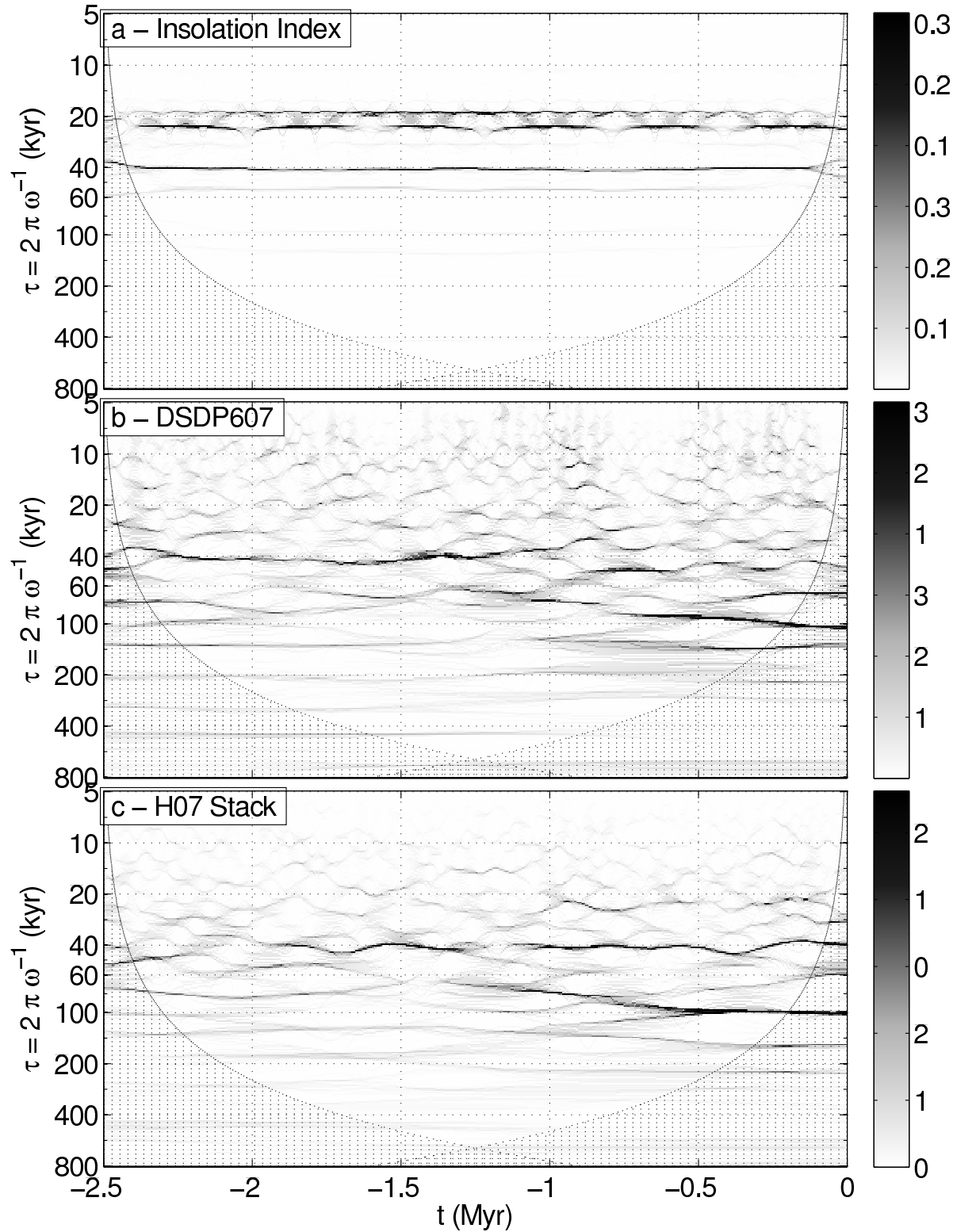


Fig. 7. Explicit time-periodicity decomposition of Synchrosqueezing spectral magnitude of (a) solar forcing index f_{SF} , and climate response in benthic $\delta^{18}O$ of (b) DSDP607 core, f_{CR1} , and (c) H07 stack, f_{CR2} .

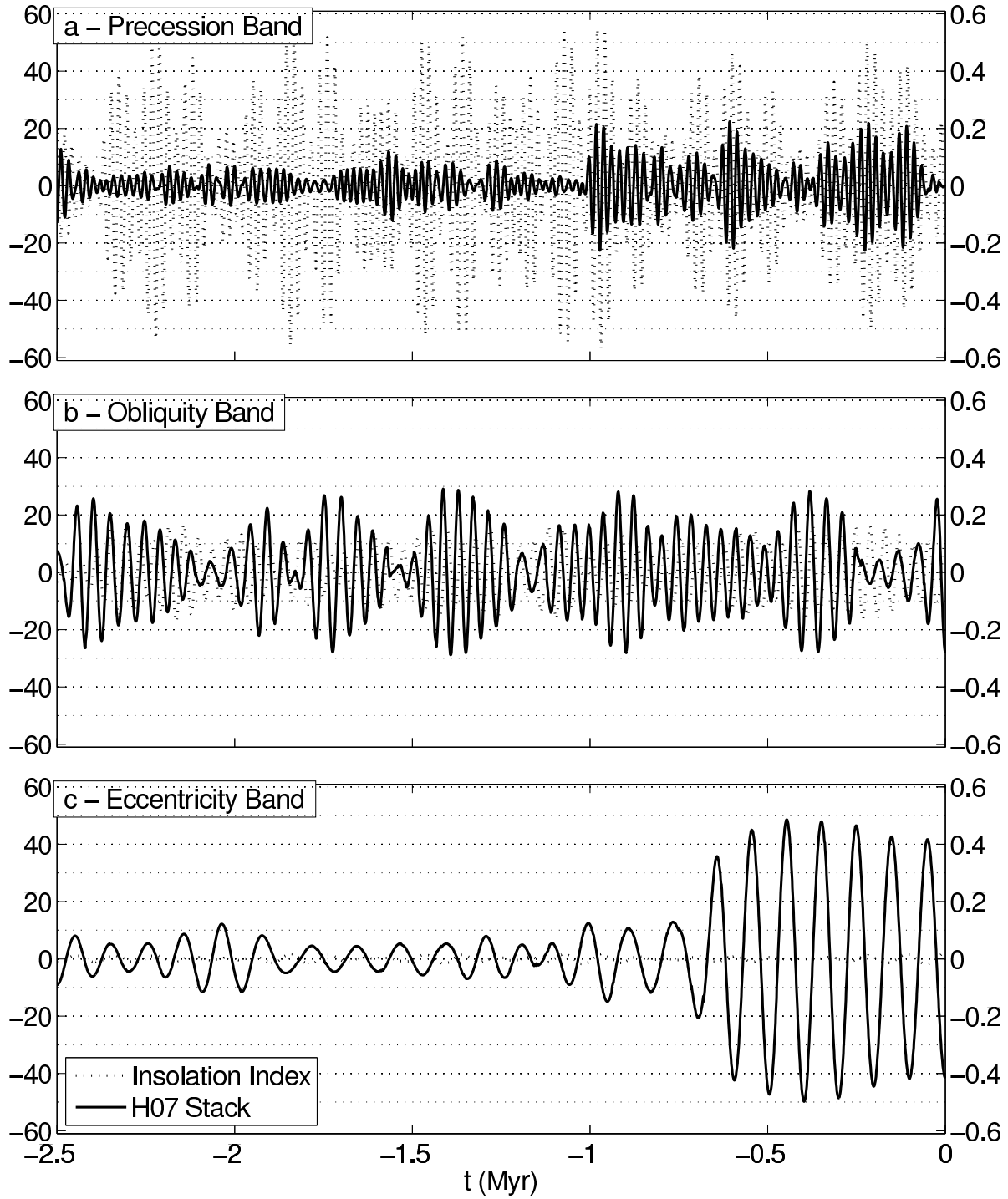


Fig. 8. Milanković orbital components extracted by the inverse Synchrosqueezing transforms of insolation index f_{SF} (gray curve with vertical scale on the left) and climate response in benthic $\delta^{18}O$ stack f_{CR2} (black curve with vertical scale on the right) over (a) precession band (integrated from 17 kyr to 25 kyr), (b) obliquity band (40 kyr - 55 kyr), and (c) eccentricity band (90 kyr - 130 kyr).

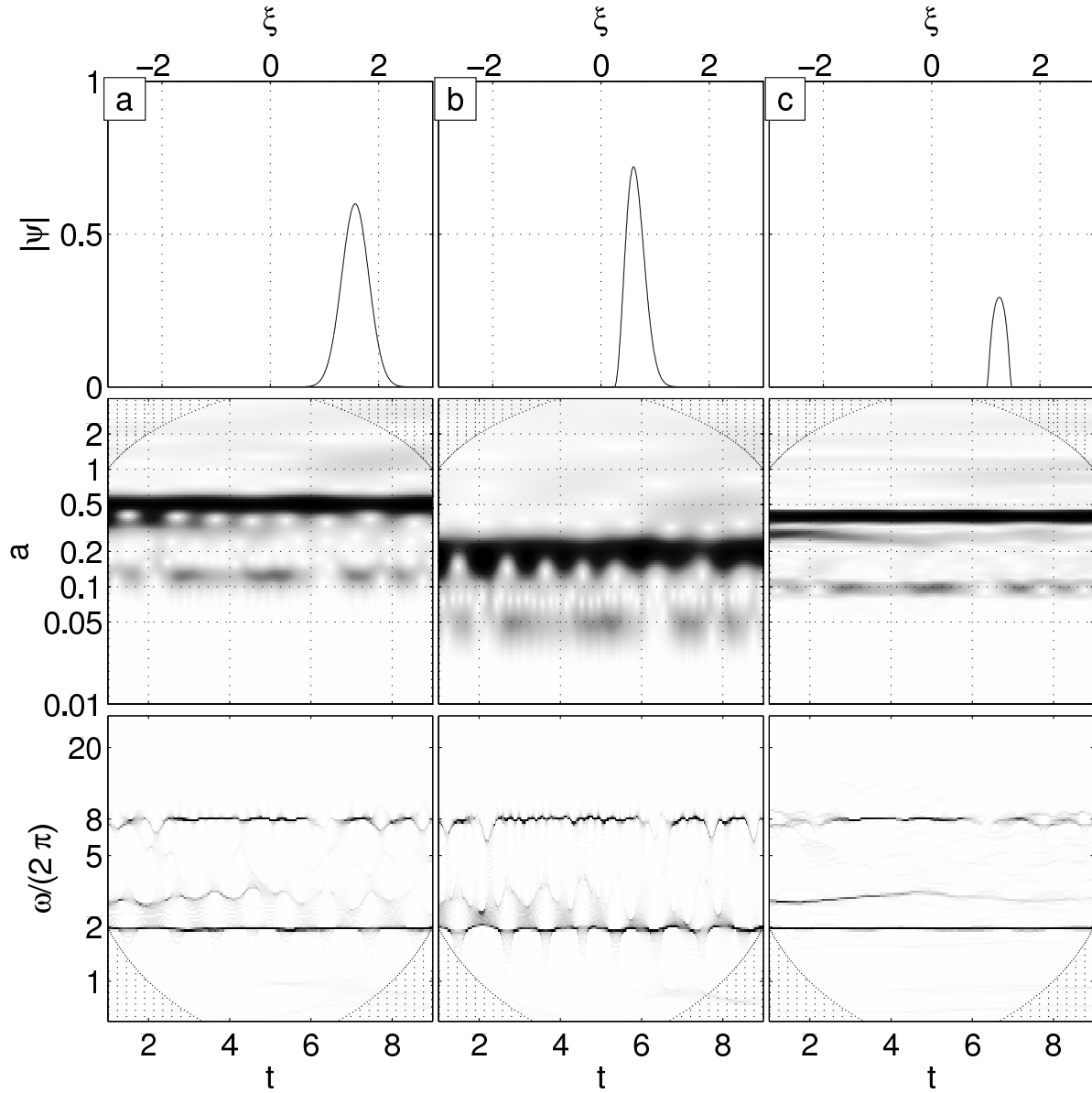


Fig. 9. Wavelet and Synchrosqueezing transforms of \tilde{f}_s . Columns (a-c) represent choice of mother wavelet $\psi_a \dots \psi_c$. Top row: $|2\hat{\psi}(4\xi)|$. Center row: $|W_{f_s}|$. Bottom row: $|T_{f_s}|$.